

Phonon-driven multipolar dynamics in spin-orbit coupled Mott insulators

Kathleen Hart,^{1,*} Ruairidh Sutcliffe,^{1,*} Gil Refael,^{2,3} and Arun Paramekanti^{1,†}

¹*Department of Physics, University of Toronto, 60 St. George Street, Toronto, ON, M5S 1A7 Canada*

²*Department of Physics, California Institute of Technology, Pasadena CA 91125, USA*

³*Institute for Quantum Information and Matter,*

California Institute of Technology, Pasadena CA 91125, USA

(Dated: May 7, 2024)

Motivated by ongoing work on pump-probe experiments and Floquet driven magnets, we theoretically study the impact of pumped and driven Einstein phonons with weak dissipation in multipolar Mott insulators. For Mott insulators with pseudospin-1/2 non-Kramers doublets hosting octupolar and quadrupolar moments, we show that pumping the \mathcal{E}_g phonon modes which couple linearly to the quadrupoles leads to characteristic chiral phonon dynamics below the octupolar ordering transition. We also explore steady states in the presence of continuously driven phonons, showing that a coherent two-phonon drive with a suitable phase choice can be used to ‘train’ octupolar order or even switch its sign. For spin-1 magnets, which host dipolar and quadrupolar moments, we show that one-phonon and two-phonon drives can generate Floquet flavor-wave excitations and induce dipolar magnetization. Our results are obtained using a generalized $SU(N)$ Monte Carlo for the multipolar degrees of freedom with numerical integration of the coupled spin-phonon equations of motion. Our work opens up pathways to explore phonon-driven dynamics in multipolar magnets.

Introduction: Shaking electrons or atoms with light has been proposed to induce remarkable Floquet many body states including topological phases in solid state crystals as well as ultracold atoms [1–7]. In recent years, rapid advances in THz optics has led to the ability to resonantly excite phonon modes in solids [8, 9], providing a remarkable pathway to probe and tune broken symmetry states including ferroelectricity [10], superconductivity [11], and magnetism [12, 13]. Experimental and theoretical work has shown that coherent phonon driving can produce fascinating effects including large effective Zeeman fields from chiral phonons [14–16], tuning magnetic orders and magnon band topology [13, 17–19], frustration breaking in dimer magnets [20, 21], nonequilibrium phase transitions [22], and high harmonic generation [23].

Recent experimental developments have extended such techniques to *multipolar* magnetic systems. Unlike dipole moments, higher order multipoles do not simply couple to conventional probes such as neutron scattering; for this reason, multipolar broken symmetries are generically termed ‘hidden orders’ [24]. Quadrupolar moments, however, directly couple to phonons, which provides a distinct route to dynamical control of multipolar order. Pump-probe and THz experiments, in which phonon modes are resonantly excited on ultrafast timescales, give evidence of multipolar dynamics and coupling to lattice vibrations [25]. Recent experiments on Ca_2RuO_4 show evidence for dynamical fluctuations into a ‘hidden’ quadrupolar-ordered state through the anomalous broadening of coherently driven phonon modes [26].

Despite this recent experimental work, the dynamical simulation of $S > 1/2$ magnets is a question that has only recently begun to be addressed [27–29]. For spin-1/2

dipole moments, spin dynamics can be described at the semiclassical level using Landau-Lifshitz equations [30]. However, for general spin- S systems with $S > 1/2$, these equations, which focus only on evolution of $SU(2)$ coherent states, do not capture the important multipolar degrees of freedom. The correct generalization uses $SU(N)$ coherent states, with $N = 2S + 1$, enabling higher-order multipole moments to be treated on equal footing with their dipole counterparts [27]. This approach can incorporate terms in the Hamiltonian beyond linear order in local spin operators, such as biquadratic exchange interactions [28, 31] and single-ion anisotropies [32, 33]. Recent work has emphasized the importance of this framework to capture key features of multipolar dynamics in inelastic neutron scattering experiments [29, 34].

In conventional dipolar magnets, local Einstein phonons can strongly couple to the spin-bilinear exchange interaction on bonds, stabilizing unusual magnetic orders in geometrically frustrated lattices such as kagome, triangular, or pyrochlore systems [36–39]. In this Letter, we construct an important extension of previous $SU(N)$ simulations of multipolar states and dynamics to include local Einstein phonons which *linearly* couple to quadrupole moments. We combine large scale $SU(N)$ Monte Carlo (MC) and spin-phonon molecular dynamics (MD) to show that one can study the coupled dynamics of phonons and multipolar orders. Using specific experimentally relevant examples, we study how kicked phonons in a pump-probe experiment can be used to probe multipolar orders, and how periodically driven phonons with weak dissipation can be used to switch multipolar order or induce Floquet copies of multipolar modes. We present illustrative results for the real time dynamics for two different systems, (i) Mott insulators with non-Kramers doublets, and (ii) Mott insulators with spin-1 moments, and point to a number of future research directions.

* These authors contributed equally to this work.

† arun.paramekanti@utoronto.ca

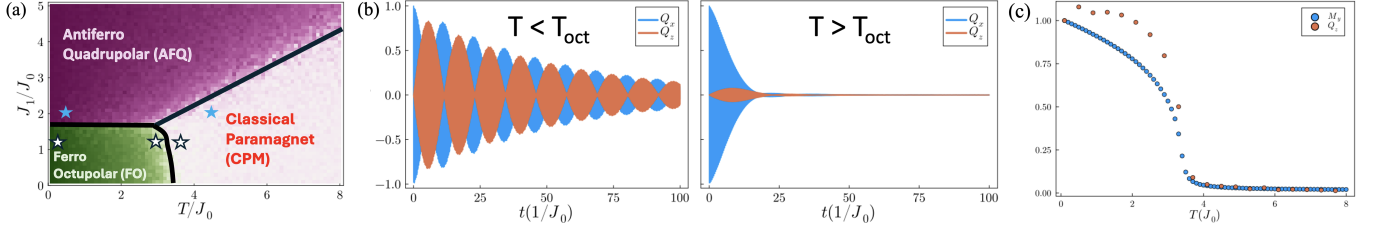


FIG. 1. (a) Phase diagram of the pseudospin-1/2 model Hamiltonian from Eq. 2 and Eq. 3 as a function of temperature and J_1/J_0 (see main text for parameters). Green region indicates the strength of the ferro-octupolar order $\langle \tau_y \rangle$, and purple region indicating the strength of antiferro-quadrupolar (AFQ) order. White stars are parameter points used in panel (b) and Fig. 2. Blue stars in the AFQ regime indicate points for which dynamics is shown in the SM [35]. (b) Phonon dynamics in pump-probe simulations induced by initial momentum kick for Q_x phonon, shown for $J_1/J_0 = 1.3$ with $T/J_0 = 0.1$ (left: $T < T_{\text{oct}}$, single domain) and $T/J_0 = 3.7$ (right: $T > T_{\text{oct}}$), averaged over 160 different initial conditions. For $T < T_{\text{oct}}$, we observe coherent transfer of energy between the Q_x and Q_z phonons, which is absent for $T > T_{\text{oct}}$. (c) Comparison showing qualitative agreement between the octupolar order parameter $M_y = \langle \tau_y \rangle$ (blue dots) and the Q_z - Q_x cross-amplitude, i.e. maximum Q_z response to Q_x pump (orange dots) as shown in panel (b); both curves are scaled by their lowest T data point.

Mott insulators of non-Kramers doublets: Non-Kramers doublets are pseudospin-1/2 degrees of freedom protected by crystalline point group symmetries which encapsulate multipolar moments. They are found in diverse quantum materials: quantum spin-ice compounds such as $\text{Pr}_2\text{Zr}_2\text{O}_7$, $\text{Pr}_2\text{Sn}_2\text{O}_7$ [40–43], Kondo lattice systems $\text{PrTi}_2\text{Al}_{20}$, $\text{PrV}_2\text{Al}_{20}$ [44–48], and Mott insulators such as oxide double perovskites $\text{Ba}_2\text{CaOsO}_6$, $\text{Ba}_2\text{MgOsO}_6$, $\text{Ba}_2\text{ZnOsO}_6$ [49–51], and vacancy ordered halide double perovskites Cs_2WCl_6 and Rb_2WCl_6 [52, 53]. We focus here on non-Kramers doublets with time-reversal even (\mathcal{T} -even) quadrupolar moments represented by pseudospin-1/2 Pauli operators (τ_x, τ_z) and a \mathcal{T} -odd octupole represented by τ_y . In the double perovskite Mott insulators, these pseudospins live on a face-centered cubic lattice, and descend from the splitting of a $J = 2$ angular momentum multiplet, with $\tau_x \propto (J_x^2 - J_y^2)$, $\tau_z \propto (3J_z^2 - J(J+1))$, and $\tau_y \propto \overline{J_x J_y J_z}$ with bar denoting operator symmetrization.

Next, consider cubic symmetry \mathcal{E}_g Einstein phonon modes at each lattice site with $x \equiv x^2 - y^2$, $z \equiv 3z^2 - r^2$. On symmetry grounds, the \mathcal{T} -odd octupole will not linearly couple to phonons, but the (τ_x, τ_z) quadrupoles can couple linearly to the phonon modes, yielding

$$H_{\text{ph}} = \sum_{\mathbf{r}, \alpha=x,z} \left[\frac{1}{2} M \Omega^2 Q_\alpha^2(\mathbf{r}) + \frac{1}{2M} P_\alpha^2(\mathbf{r}) \right], \quad (1)$$

$$H_{\text{sp-ph}} = -\lambda \sum_{\mathbf{r}} [Q_x(\mathbf{r}) \tau_{\text{rx}} + Q_z(\mathbf{r}) \tau_{\text{rz}}]. \quad (2)$$

Here, (Q_α, P_α) are the normal mode coordinates and momenta, and Ω, M represent the frequency and mass, and λ is the spin-phonon coupling.

Symmetries also dictate the following Hamiltonian de-

scribing pseudospin exchange interactions

$$\begin{aligned} H_{\text{sp}} = \sum_{\langle \mathbf{r}, \mathbf{r}' \rangle} & [-J_0 \tau_{\mathbf{r}y} \tau_{\mathbf{r}'y} + J_1 (\cos^2 \phi_{\mathbf{r}\mathbf{r}'} + \gamma \sin^2 \phi_{\mathbf{r}\mathbf{r}'}) \tau_{\mathbf{r}z} \tau_{\mathbf{r}'z} \\ & + J_1 (1 - \gamma) \sin \phi_{\mathbf{r}\mathbf{r}'} \cos \phi_{\mathbf{r}\mathbf{r}'} (\tau_{\mathbf{r}x} \tau_{\mathbf{r}'z} + \tau_{\mathbf{r}z} \tau_{\mathbf{r}'x}) \\ & + J_1 (\sin^2 \phi_{\mathbf{r}\mathbf{r}'} + \gamma \cos^2 \phi_{\mathbf{r}\mathbf{r}'}) \tau_{\mathbf{r}x} \tau_{\mathbf{r}'x}] \end{aligned} \quad (3)$$

where $\phi_{ij} = \{0, 2\pi/3, 4\pi/3\}$ correspond to nearest neighbors $\langle \mathbf{r}\mathbf{r}' \rangle$ in the $\{XY, YZ, ZX\}$ planes.

(i) *Equilibrium phase diagram.*— We begin by constructing the equilibrium phase diagram of the full model $H = H_{\text{sp}} + H_{\text{ph}} + H_{\text{sp-ph}}$ in the presence of coupling to the cubic \mathcal{E}_g phonon modes. For this purpose, it is useful to define a length scale $a = 0.01a_0$, where $a_0 \approx 4 \text{ \AA}$ is the cubic lattice constant; in terms of this, a phonon amplitude $Q_\alpha/a \sim 1$ corresponds to a 1% dynamical strain. Based on density functional and dynamical mean field theory studies, we determine $\Omega/J_0 \sim 80$, $\lambda a/J_0 \approx 5$, $\hbar^2/(2M J_0 a^2) \approx 80$, $M \Omega^2 a^2/(2J_0) \approx 20$, $\gamma \approx -0.4$; see SM [35] for details. Fig. 1(a) displays the phase diagram obtained from our MC simulations (on system size with 10^3 sites) as we vary the temperature T/J_0 and quadrupolar exchange J_1/J_0 . We find a high temperature paramagnetic phase, a low temperature ferro-octupolar ordered phase for $J_1/J_0 \lesssim 1.8$ and an antiferroquadrupolar phase with wavevector $(\pi, \pi, 0)$ (and equivalent) for $J_1/J_0 \gtrsim 1.8$. At low T , phonon displacements are absent in the ferro-octupolar phase, while the antiferroquadrupolar phase shows small displacements $Q_\alpha \sim 0.1a$ which track the local quadrupole order.

(ii) *Pump-probe dynamics.*— In pump-probe experiments [26], an incoming pump beam can excite the even-parity cubic \mathcal{E}_g phonon modes via a two-photon Raman transition or via non-linear phononics, and their subsequent dynamics can potentially provide useful information about broken symmetries in the system. To simulate such pump-probe dynamics, we use equilibrated Monte Carlo configurations of the spins and phonon coordinates as initial conditions, and kick the Q_x phonon by choosing

its momenta from a *displaced* Maxwell thermal distribution. This models the pump-beam as a uniform impulsive momentum kick to the phonon at all sites [26]; we check that our quench leads to a maximum phonon displacement $Q_\alpha/a \lesssim 1$ over the time evolution. With these initial conditions, we compute the Schrodinger evolution for the pseudospin wavefunction together with Newton's laws for the classical phonons, and track time evolution of observables averaged over a large number of initial Monte Carlo configurations out to times $t = 100/J_0 = 8000/\Omega$ for system sizes up to 10^3 sites (see SM [35] for details). We have included a weak damping of the \mathcal{E}_g phonons, incorporating an additional term $(-\eta P_\alpha)$ in the force equation dP_α/dt , to capture energy dissipation to the bath of acoustic phonon modes. This mechanism of energy damping via phonons is more relevant to Mott insulators than Gilbert damping of spin modes which plays a role in metallic magnets. Fig. 1(b) shows the time evolution of the phonon displacements $Q_x(t)$ and $Q_z(t)$ when we give an impulsive kick to the Q_x phonon at time $t = 0$ in the octupolar ordered and paramagnetic phases. The rapid oscillations of the Q_x, Q_z modes at the phonon frequency are not visible for the long time scales shown in the plot, but are shown in the SM [35]. Remarkably, the presence of octupolar broken symmetry for $T < T_{\text{oct}}$ leads to coherent energy oscillations between the two phonon modes on time scales $\sim 5/J_0$, while such energy oscillations are rapidly dephased or very weak in the paramagnet and quadrupolar phases. As shown in Fig. 1(c), the maximum cross-amplitude, i.e. the highest amplitude of the Q_z oscillations with an impulsive kick to the Q_x phonon, serves as a direct probe of the octupolar order parameter. We can understand this with a mean field model of the dynamics (see SM [35]), where the octupolar ordered state leads to a Weiss field along τ_y , and the pumped phonon leads to tipping of the initial pseudospin state away from τ_y . This leads to coherent pseudospin precession around τ_y -axis, serving as a conduit to transfer energy from Q_x to Q_z and back. Phonon pump-probe spectroscopy thus serves a useful tool to probe hidden multipolar orders.

(iii) *Training and switching multipolar order.*— We next explore how a simultaneous coherent drive of both cubic \mathcal{E}_g phonon modes can be used to control octupolar ordering. We consider a time-dependent Hamiltonian $H_{\text{drive}}^{\text{ph}} = -A \sum_{\mathbf{r}} [Q_x(\mathbf{r}) \cos \Omega t + Q_z(\mathbf{r}) \cos(\Omega t - \phi)]$ which describes the coherent driving of the degenerate Q_x, Q_z phonons on resonance, and explore its impact on the pseudospins. Fig. 2(a) shows the effect of this resonant drive in the paramagnetic phase, averaged over 320 initial MC configurations, for phases $\phi = (0, \pm\pi/4, \pm\pi/2)$, where we include weak phonon dissipation to allow the system to thermalize and reach steady state. We find that depending on the relative phase, the coherent drive can induce octupolar order $\langle \tau_y \rangle$ of either sign in the paramagnetic phase. Previous work has shown, using an effective rate equation approach, that time-dependent chiral driving of phonons

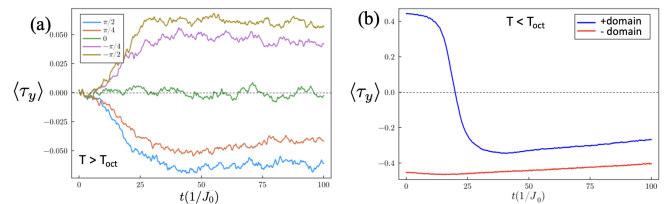


FIG. 2. Dynamics of $\langle \tau_y \rangle$ in the presence of phase coherent two-phonon drive with weak dissipation (see text for details). (a) In the paramagnet $T = 1.1T_{\text{oct}}$, with amplitude $A = 0.05$ (resonant phonon amplitude $Q_0 \approx 0.5a$) and different phase differences $\phi \in [-\pi/2, \pi/2]$, showing that two-phonon drive can be used ‘train’ the sign of octupolar order. (b) In the ferro-octupolar ordered phase $T = 0.8T_{\text{oct}}$, with a larger amplitude $A = 0.2$ (resonant phonon amplitude $Q_0 \approx 1.5a$) showing that with a suitable choice of phase $\phi = \pi/2$ it can be used to switch from positive to negative octupolar order.

can pump angular momentum and induce effective fields for dipolar $4f$ magnets [14]. Our work provides a non-trivial generalization of this idea to multipolar order. To understand this physics, we note that the phonons linearly couple to the quadrupoles, so we consider a proxy Hamiltonian which directly drives quadrupoles as $H_{\text{drive}}^{\text{sp}} = -A_{\text{eff}} \sum_{\mathbf{r}} (\tau_{\mathbf{rx}} \cos \Omega t + \tau_z \cos(\Omega t - \phi))$. Here, the effective field $A_{\text{eff}} = \lambda Q_0$ with Q_0 being the driven phonon amplitude (which depends on the drive strength A). We study this Floquet problem using a Magnus expansion in the lab frame which is justified since $\Omega \gg J_0$, i.e. the phonon dynamics is much faster than the pseudospin dynamics [1, 7, 54]. We find, in standard notation,

$$H_{\text{drive},0}^{\text{sp}} = 0; \quad H_{\text{drive},\pm}^{\text{sp}} = -\frac{\lambda Q_0}{2} \sum_{\mathbf{r}} (\tau_{\mathbf{rx}} + e^{\mp i\phi} \tau_{\mathbf{rz}}) \quad (4)$$

$$H_{\text{drive}}^{\text{sp,eff}} = \frac{1}{\Omega} [H_{\text{drive},+}^{\text{sp}}, H_{\text{drive},-}^{\text{sp}}] = \frac{\lambda^2 Q_0^2}{\Omega} \sin \phi \sum_{\mathbf{r}} \tau_{\mathbf{ry}} \quad (5)$$

This phonon-induced effective field in $H_{\text{drive}}^{\text{sp,eff}}$, $(-\lambda^2 Q_0^2/\Omega) \sin \phi$, explains the induced ϕ -dependent octupolar order for $T > T_{\text{oct}}$ shown in Fig. 2(a).

We next ask if this same mechanism can be used to also switch the sign of octupolar order for $T < T_{\text{oct}}$. Fig. 2(b) shows the impact of the two-phonon coherent drive for $\phi = \pi/2$ at $T/T_{\text{oct}} = 0.8$ for a larger amplitude drive than we used above. Using a drive which leads to a resonant phonon amplitude $Q_0 \sim 1.5a$, we find that octupolar order in the positive domain switches sign, while the octupolar order in the negative domain is nearly unaffected. In order for this switching to occur, the phonon-induced field $(-\lambda^2 Q_0^2/\Omega) \sin \phi$ must overcome the octupolar Weiss field in the ordered phase. Plugging in numbers, we find that the phonon-induced field is too small to flip pseudospins deep inside a domain, but it can happen at domain walls where the Weiss field is strongly suppressed. Thus, negative domains must grow by flipping pseudospins at the boundary until the entire octupolar $\langle \tau_y \rangle$ flips (see SM [35] for details and an effective mean

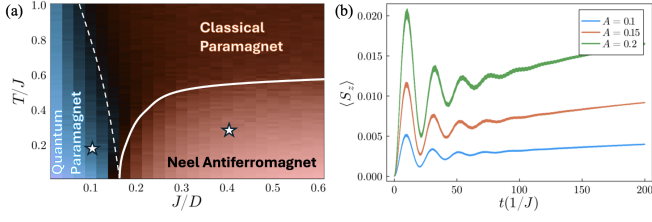


FIG. 3. (a) Equilibrium phase diagram of the spin-1 model described by Eq. (6) and Eq.(8) (see text for details). We find a quantum phase transition at $J/D \approx 0.18$ separating a quantum paramagnet with $S_z = 0$ from a Néel ordered antiferromagnet, with a classical paramagnet at high temperature. Solid and dashed lines indicate phase transition and crossover respectively. Color scale shows the average spin-dipole length in the different phases. Stars indicate points where we present simulation results from phonon-driven dynamics. (b) Time evolution of S_z magnetization induced by coherent two-phonon drive in the quantum paramagnet.

field model). The slow evolution of $\langle \tau_y \rangle$ at late times, and the nearly unchanged $\langle \tau_y \rangle$ in the ‘-’ domain, indicate that heating effects are weak at these timescales.

Spin-1 Mott insulators: We next turn to spin-1 magnets with dipolar and quadrupolar degrees of freedom which can display rich phase diagrams including spin nematics, and coexisting dipolar-quadrupolar orders, driven by the competition between dipolar spin exchange, biquadratic interactions, and single-ion anisotropies. We consider the simple Hamiltonian

$$H_{\text{sp}} = \sum_{\langle \mathbf{r}, \mathbf{r}' \rangle} J_{\mathbf{r}\mathbf{r}'} \mathbf{S}(\mathbf{r}) \cdot \mathbf{S}(\mathbf{r}') + D \sum_{\mathbf{r}} S_z^2(\mathbf{r}) \quad (6)$$

where $J_{\mathbf{r}\mathbf{r}'}$ is the Heisenberg exchange and $D > 0$ is a single-ion anisotropy. Such a model, with large $D > 0$, favors a quadrupolar ground state with $S_z = 0$ at each site, which may be relevant to diamond lattice Ni^{2+} compounds [55, 56]. A similar model on the tetragonal lattice, with $J \sim 0.25 \text{ meV}$ for nearest neighbors in the XY plane, interlayer coupling $J' \sim 0.1J$, and $D \sim 1.4 \text{ meV}$ captures the low energy magnetism in $\text{Ba}_2\text{FeSi}_2\text{O}_7$, showing quasi-2D Néel order coexisting with a significant quadrupolar moment [29].

Here, we consider the spin model in Eq. 6 on the tetragonal lattice, and couple it to \mathcal{E}_g phonons (Q_{xz}, Q_{yz}) (for D_{4h} symmetry), via

$$H_{\text{ph}} = \sum_{\mathbf{r}, \alpha=xz, yz} \left[\frac{1}{2} M \Omega^2 Q_\alpha^2(\mathbf{r}) + \frac{1}{2M} P_\alpha^2(\mathbf{r}) \right], \quad (7)$$

$$H_{\text{sp-ph}} = \lambda \sum_{\mathbf{r}} [Q_{xz}(\mathbf{r}) T_{xz}(\mathbf{r}) + Q_{yz}(\mathbf{r}) T_{yz}(\mathbf{r})], \quad (8)$$

where $T_{\mu\nu} = (S_\mu S_\nu + S_\nu S_\mu)$ are quadrupole moments. We set $J'/J = 0.1$, $\Omega/J \approx 40$, $\lambda a/J = 2.5$, $\hbar^2/(2MJa^2) = 80$, $M\Omega^2 a^2/(2J) \approx 5$. Using $SU(3)$ MC simulations incorporating phonons, we have determined the equilibrium phase diagram of this spin-phonon model as shown

in Fig. 3(a), largely in agreement with previous work [29] for our choice of weak spin-phonon coupling $\lambda a/J = 2.5$. We next use the $SU(3)$ spin-phonon dynamics approach to study the phonon-driven magnetization and Floquet flavor-wave excitations. Technically, it is convenient to implement this using $SU(3)$ Gell-Mann matrices [35].

(i) *Phonon induced magnetization.*— We first explore the quantum paramagnetic phase, and study the effect of a coherent drive of both tetragonal \mathcal{E}_g phonons with $H_{\text{drive}}^{\text{ph}} = -A \sum_{\mathbf{r}} (Q_{xz}(\mathbf{r}) \cos \Omega t + Q_{yz}(\mathbf{r}) \sin \Omega t)$. Fig. 3(b) shows the phonon induced uniform S_z magnetization which settles to a near steady state after the initial oscillatory transients. We can capture this steady state physics using a Magnus expansion, justified by the phonon frequency $\Omega \gg J, J', D$. Since the phonons couple linearly to the spin quadrupoles, we first replace the phonon drive by an effective spin drive, $H_{\text{drive}}^{\text{sp}} = -A_{\text{eff}} \sum_{\mathbf{r}} (T_{xz} \cos(\Omega t) + T_{yz} \sin(\Omega t))$. Here, the effective field $A_{\text{eff}} = \lambda Q_0$ with Q_0 being the driven phonon amplitude (which depends on the drive strength A). The leading order in $1/\Omega$ effective Hamiltonian is then $H_{\text{drive}}^{\text{eff,ph}} = -(A_{\text{eff}}^2/2\Omega) S_z(\mathbf{r})$. The effective field ($A_{\text{eff}}^2/2\Omega$) explains both the induced magnetization and its scaling with the drive amplitude A in Fig. 3(b).

(ii) *Floquet flavor-wave excitations.*— Finally, we explore Néel antiferromagnetic ground state, and study the effect of driving a single \mathcal{E}_g phonon (Q_{xz}) of this tetragonal crystal, with $H_{\text{drive}}^{\text{ph}} = -A \sum_{\mathbf{r}} Q_{xz}(\mathbf{r}) \cos \Omega t$. Using the $SU(3)$ spin dynamics coupled to the phonons, we have computed the dynamical spin structure factor $\mathcal{S}_{\text{dr}}(\mathbf{q}, \omega)$ for the driven spin model (see SM [35]). Fig. 4(a) shows the low energy $\mathcal{S}_{\text{dr}}(\mathbf{q}, \omega)$, revealing a flavor-wave spectrum with two highly dispersive trans-

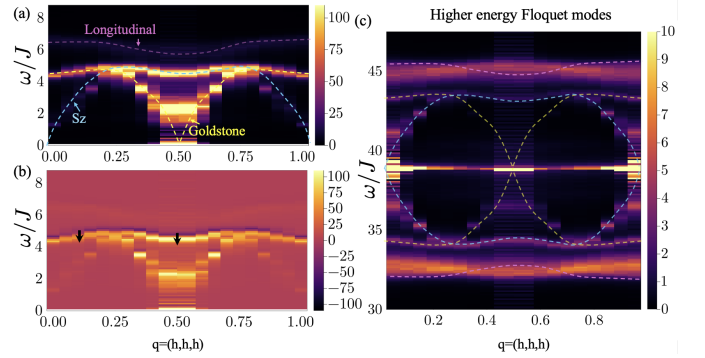


FIG. 4. (a) Dynamical spin structure $\mathcal{S}_{\text{dr}}(\mathbf{q}, \omega)$ in the presence of Q_{xz} -phonon drive in the Néel antiferromagnet revealing three branches of flavor-wave modes (dashed lines are guide to the eye). The two transverse modes are labelled S_z and ‘Goldstone’ which correspond to out-of-plane and in-plane fluctuations. (b) The difference spectrum $\mathcal{S}_{\text{dr}}(\mathbf{q}, \omega) - \mathcal{S}_{\text{eq}}(\mathbf{q}, \omega)$, with small black arrows highlighting the weak downward renormalization of the mode energies induced by the phonon drive. (c) At higher energies, we find Floquet copies of the low energy flavor-wave modes (dashed lines) with both \pm branches being visible since $\mathcal{S}_{\text{dr}}(\mathbf{q}, \omega) = \mathcal{S}_{\text{dr}}(\mathbf{q}, -\omega)$. See text for details.

verse modes and a higher energy weakly dispersing longitudinal mode. As a guide to the eye, we have shown dashed lines to trace these dispersions; these are qualitatively similar to previous results obtained in the absence of spin-phonon coupling [29, 34]. This result for $\mathcal{S}_{\text{dr}}(\mathbf{q}, \omega)$ is very close to the equilibrium spin-phonon coupled result $\mathcal{S}_{\text{eq}}(\mathbf{q}, \omega)$ [35] due to the weak drive amplitude A used in these simulations. Fig. 4(b) highlights the change by plotting the difference spectrum $\mathcal{S}_{\text{dr}}(\mathbf{q}, \omega) - \mathcal{S}_{\text{eq}}(\mathbf{q}, \omega)$, which reveals a small downward shift in the mode energies in the driven case. A second-order Magnus expansion explains this downward spectral shift as arising from a downward renormalization of $J_{\text{rr}'}$ and D ; see SM [35]. Finally, Fig. 4(c) plots $\mathcal{S}_{\text{dr}}(\mathbf{q}, \omega)$ for higher energies in the vicinity of the phonon energy $\Omega/J \sim 40$, showing clear signatures of phonon-induced Floquet copies of the flavor-wave spectrum as well as a signature of the flat phonon mode itself in the magnetic $\mathcal{S}_{\text{dr}}(\mathbf{q}, \omega)$. The higher energy Floquet modes have lower intensity, and show up as both \pm branches of the dispersion centered around the phonon energy, since inversion symmetry fixes $\mathcal{S}(\mathbf{q}, -\omega) = \mathcal{S}(\mathbf{q}, \omega)$, and ignoring spectral intensities $\mathcal{S}(\mathbf{q}, -\omega) \sim \mathcal{S}(\mathbf{q}, \Omega - \omega)$. One aspect of the higher energy Floquet modes we have not understood is the difference in dispersion of the longitudinal mode in the higher energy Floquet spectrum when compared with the low energy regime; see highest energy dashed line in Fig. 4(c). We tentatively attribute this difference to phonon dissipation effects but hope to clarify this in future work. These Floquet flavor-wave excitations, which are driven dipolar-quadrupolar modes, could po-

tentially be detected for $\mathbf{q} = 0$ using THz spectroscopy. A more challenging experiment, analogous to time and angle resolved photoemission spectroscopy used to observe electronic Floquet states in topological insulators and graphene [57–59], would be inelastic neutron scattering in the presence of driven phonons [60].

Summary: We have devised a numerical tool to explore how weakly dissipative Einstein phonons couple to multipolar degrees of freedom in Mott insulators, and how this can be used to study the dynamics and control of hidden orders. Using both pump-probe schemes and continuous driving with dissipation, we have shown ways to detect octupolar order, switch octupolar order, generate magnetization in a quadrupolar quantum paramagnet, and uncover Floquet flavor-wave modes in the dynamical structure factor of a driven spin-1 magnet. Our work should provide an impetus for exploring theoretical and experimental work in the field of driven quantum magnets, including driven spin-ice systems and other frustrated magnets, as well as opening up avenues to explore non-equilibrium multipolar matter.

This research was funded by an NSERC Discovery Grant (AP), an Ontario Graduate Scholarship (KH), and an NSERC CGS-D fellowship (RS). We thank Sreekar Voleti for initial collaboration on this project. KH and RS thank Emily Zhang and William Bateman-Hemphill for helpful discussions, and AP thanks Cristian Batista for a useful conversation about $SU(N)$ spin dynamics. Numerical computations were performed on the Niagara supercomputer at the SciNet HPC Consortium and the Digital Research Alliance of Canada.

-
- [1] T. Oka and S. Kitamura, Floquet engineering of quantum materials, Annual Review of Condensed Matter Physics **10**, 387 (2019).
 - [2] M. S. Rudner and N. H. Lindner, Band structure engineering and non-equilibrium dynamics in floquet topological insulators, Nature Reviews Physics **2**, 229 (2020).
 - [3] A. Eckardt, Colloquium: Atomic quantum gases in periodically driven optical lattices, Rev. Mod. Phys. **89**, 011004 (2017).
 - [4] N. H. Lindner, G. Refael, and V. Galitski, Floquet topological insulator in semiconductor quantum wells, Nature Physics **7**, 490 (2011).
 - [5] M. Rodriguez-Vega, M. Vogl, and G. A. Fiete, Low-frequency and moirfloquet engineering: A review, Annals of Physics **435**, 168434 (2021), special issue on Philip W. Anderson.
 - [6] N. H. Lindner, D. L. Bergman, G. Refael, and V. Galitski, Topological floquet spectrum in three dimensions via a two-photon resonance, Phys. Rev. B **87**, 235131 (2013).
 - [7] M. Bukov, L. D'Alessio, and A. Polkovnikov, Universal high-frequency behavior of periodically driven systems: from dynamical stabilization to floquet engineering, Advances in Physics **64**, 139 (2015).
 - [8] M. Först, C. Manzoni, S. Kaiser, Y. Tomioka, Y. Tokura, R. Merlin, and A. Cavalleri, Nonlinear phononics as an ultrafast route to lattice control, Nature Physics **7**, 854 (2011).
 - [9] D. Nicoletti and A. Cavalleri, Nonlinear light-matter interaction at terahertz frequencies, Advances in Optics and Photonics **8**, 401 (2016).
 - [10] R. Mankowsky, A. von Hoegen, M. Först, and A. Cavalleri, Ultrafast reversal of the ferroelectric polarization, Phys. Rev. Lett. **118**, 197601 (2017).
 - [11] B. Liu, M. Först, M. Fechner, D. Nicoletti, J. Porras, T. Loew, B. Keimer, and A. Cavalleri, Pump frequency resonances for light-induced incipient superconductivity in $\text{YbBa}_2\text{Cu}_3\text{O}_{6.5}$, Phys. Rev. X **10**, 011053 (2020).
 - [12] A. S. Disa, M. Fechner, T. F. Nova, B. Liu, M. Först, D. Prabhakaran, P. G. Radaelli, and A. Cavalleri, Polarizing an antiferromagnet by optical engineering of the crystal field, Nature Physics **16**, 937 (2020).
 - [13] A. S. Disa, J. Curtis, M. Fechner, A. Liu, A. von Hoegen, M. Först, T. F. Nova, P. Narang, A. Maljuk, A. V. Boris, B. Keimer, and A. Cavalleri, Photo-induced high-temperature ferromagnetism in YtIO_3 , Nature **617**, 73 (2023).
 - [14] D. M. Juraschek, T. Neuman, and P. Narang, Giant effective magnetic fields from optically driven chiral phonons in 4 f paramagnets, Physical Review Research **4**, 013129 (2022).
 - [15] F. G. Hernandez, A. Baydin, S. Chaudhary, F. Tay, I. Katayama, J. Takeda, H. Nojiri, A. K. Okazaki, P. H.

- Rappl, E. Abramof, *et al.*, Chiral phonons with giant magnetic moments in a topological crystalline insulator, arXiv preprint arXiv:2208.12235 (2022).
- [16] S. Chaudhary, D. M. Juraschek, M. Rodriguez-Vega, and G. A. Fiete, Giant effective magnetic moments of chiral phonons from orbit-lattice coupling (2023), arXiv:2306.11630 [cond-mat.mes-hall].
- [17] J. B. Curtis, A. Disa, M. Fechner, A. Cavalleri, and P. Narang, Dynamics of photoinduced ferromagnetism in oxides with orbital degeneracy, *Phys. Rev. Res.* **5**, 013204 (2023).
- [18] M. Rodriguez-Vega, Z.-X. Lin, A. Leonardo, A. Ernst, G. Chaudhary, M. G. Vergniory, and G. A. Fiete, Phonon-mediated dimensional crossover in bilayer Criz, *Phys. Rev. B* **102**, 081117 (2020).
- [19] M. Rodriguez-Vega, Z.-X. Lin, A. Leonardo, A. Ernst, M. G. Vergniory, and G. A. Fiete, Light-driven topological and magnetic phase transitions in thin layer antiferromagnets, *The Journal of Physical Chemistry Letters* **13**, 4152 (2022).
- [20] F. Giorgianni, B. Wehinger, S. Allenspach, N. Colonna, C. Vicario, P. Puphal, E. Pomjakushina, B. Normand, and C. Rüegg, Ultrafast frustration breaking and magnetophononic driving of singlet excitations in a quantum magnet, *Phys. Rev. B* **107**, 184440 (2023).
- [21] F. Giorgianni, B. Wehinger, S. Allenspach, N. Colonna, C. Vicario, P. Puphal, E. Pomjakushina, B. Normand, and C. Rüegg, Ultrafast frustration breaking and magnetophononic driving of singlet excitations in a quantum magnet, *Phys. Rev. B* **107**, 184440 (2023).
- [22] M. Yarmohammadi, M. Bukov, V. Oganesyan, and M. H. Kolodrubetz, Laser-enhanced magnetism in smfe_{o3} (2023), arXiv:2308.14939 [cond-mat.mtrl-sci].
- [23] N. M. Allafi, M. H. Kolodrubetz, M. Bukov, V. Oganesyan, and M. Yarmohammadi, Spin high-harmonic generation through terahertz laser-driven phonons (2024), arXiv:2404.05830 [cond-mat.str-el].
- [24] J. A. Mydosh, P. M. Oppeneer, and P. S. Riseborough, Hidden order and beyond: an experimental/theoretical overview of the multifaceted behavior of uru₂si₂, *Journal of Physics: Condensed Matter* **32**, 143002 (2020).
- [25] F. Giorgianni, B. Wehinger, S. Allenspach, N. Colonna, C. Vicario, P. Puphal, E. Pomjakushina, B. Normand, and C. Rüegg, Ultrafast frustration breaking and magnetophononic driving of singlet excitations in a quantum magnet, *Physical Review B* **107**, 184440 (2023).
- [26] H. Ning, O. Mehio, X. Li, M. Buchhold, M. Driesse, H. Zhao, G. Cao, and D. Hsieh, A coherent phonon-induced hidden quadrupolar ordered state in ca₂ruo₄, *Nature Communications* **14**, 8258 (2023).
- [27] D. Dahlbom, H. Zhang, C. Miles, X. Bai, C. D. Batista, and K. Barros, Geometric integration of classical spin dynamics via a mean-field schrödinger equation, *Physical Review B* **106**, 054423 (2022).
- [28] K. Remund, R. Pohle, Y. Akagi, J. Romhányi, and N. Shannon, Semi-classical simulation of spin-1 magnets, *Physical Review Research* **4**, 033106 (2022).
- [29] S.-H. Do, H. Zhang, D. A. Dahlbom, T. J. Williams, V. O. Garlea, T. Hong, T.-H. Jang, S.-W. Cheong, J.-H. Park, K. Barros, *et al.*, Understanding temperature-dependent su (3) spin dynamics in the s= 1 antiferromagnet ba₂fesi₂o₇, *npj Quantum Materials* **8**, 5 (2023).
- [30] M. Lakshmanan, The fascinating world of the landau-lifshitz-gilbert equation: an overview, *Philosophical Transactions of the Royal Society A: Mathematical, Physical and Engineering Sciences* **369**, 1280 (2011).
- [31] E. Stoudenmire, S. Trebst, and L. Balents, Quadrupolar correlations and spin freezing in s= 1 triangular lattice antiferromagnets, *Physical Review B* **79**, 214436 (2009).
- [32] D. Dahlbom, C. Miles, H. Zhang, C. D. Batista, and K. Barros, Langevin dynamics of generalized spins as su (n) coherent states, *Physical Review B* **106**, 235154 (2022).
- [33] D. Dahlbom, H. Zhang, Z. Laraib, D. M. Pajerowski, K. Barros, and C. Batista, Renormalized classical theory of quantum magnets, arXiv preprint arXiv:2304.03874 (2023).
- [34] S.-H. Do, H. Zhang, T. J. Williams, T. Hong, V. O. Garlea, J. Rodriguez-Rivera, T.-H. Jang, S.-W. Cheong, J.-H. Park, C. D. Batista, *et al.*, Decay and renormalization of a longitudinal mode in a quasi-two-dimensional antiferromagnet, *Nature communications* **12**, 5331 (2021).
- [35] See Supplemental Material for details about the (i) *SU(N)* Monte Carlo and molecular dynamics method including phonons, (ii) additional results and (iii) toy model mean field dynamics.
- [36] D. L. Bergman, R. Shindou, G. A. Fiete, and L. Balents, Models of degeneracy breaking in pyrochlore antiferromagnets, *Phys. Rev. B* **74**, 134409 (2006).
- [37] F. Wang and A. Vishwanath, Spin phonon induced collinear order and magnetization plateaus in triangular and kagome antiferromagnets: Applications to cu₂e₂, *Physical review letters* **100**, 077201 (2008).
- [38] A. Szasz, C. Wang, and Y.-C. He, Phase diagram of a bilinear-biquadratic spin-1 model on the triangular lattice from density matrix renormalization group simulations, *Physical Review B* **106**, 115103 (2022).
- [39] Y. Watanabe, M. Gen, T. Kurumaji, Y. Tokunaga, and T.-h. Arima, Magnetic-field-induced antiferromagnetic-antiferromagnetic phase transition in quasi-two-dimensional multiferroic material ba₂fesi₂o₇, *Journal of the Physical Society of Japan* **92**, 014701 (2023).
- [40] K. Matsuhira, C. Sekine, C. Paulsen, M. Wakeshima, Y. Hinatsu, T. Kitazawa, Y. Kiuchi, Z. Hiroi, and S. Takagi, Spin freezing in the pyrochlore antiferromagnet pr₂zr₂o₇, in *Journal of Physics: Conference Series*, Vol. 145 (IOP Publishing, 2009) p. 012031.
- [41] K. Kimura, S. Nakatsuji, J. Wen, C. Broholm, M. Stone, E. Nishibori, and H. Sawa, Quantum fluctuations in spin-ice-like pr₂zr₂o₇, *Nature communications* **4**, 1934 (2013).
- [42] S. Lee, S. Onoda, and L. Balents, Generic quantum spin ice, *Physical Review B* **86**, 104412 (2012).
- [43] A. S. Patri, M. Hosoi, S. Lee, and Y. B. Kim, Theory of magnetostriction for multipolar quantum spin ice in pyrochlore materials, *Physical Review Research* **2**, 033015 (2020).
- [44] A. Sakai, K. Kuga, and S. Nakatsuji, Superconductivity in the ferroquadrupolar state in the quadrupolar kondo lattice prti₂al₂₀, *Journal of the Physical Society of Japan* **81**, 083702 (2012).
- [45] T. Taniguchi, M. Yoshida, H. Takeda, M. Takigawa, M. Tsujimoto, A. Sakai, Y. Matsumoto, and S. Nakatsuji, Nmr observation of ferro-quadrupole order in prti₂al₂₀, *Journal of the Physical Society of Japan* **85**, 113703 (2016).
- [46] S. Lee, S. Trebst, Y. B. Kim, and A. Paramekanti, Landau theory of multipolar orders in pr (y) ₂ x ₂₀ kondo materials (y= ti, v, rh, ir; x= al, zn), *Physical Review B*

- 98**, 134447 (2018).
- [47] F. Freyer, J. Attig, S. Lee, A. Paramakanti, S. Trebst, and Y. B. Kim, Two-stage multipolar ordering in $\text{PrTi}_2\text{Al}_{20}$ kondo materials, *Physical Review B* **97**, 115111 (2018).
 - [48] A. S. Patri, A. Sakai, S. Lee, A. Paramakanti, S. Nakatsuji, and Y. B. Kim, Unveiling hidden multipolar orders with magnetostriiction, *Nature Communications* **10**, 4092 (2019).
 - [49] D. D. Maharaj, G. Sala, M. B. Stone, E. Kermarrec, C. Ritter, F. Fauth, C. A. Marjerrison, J. E. Greedan, A. Paramakanti, and B. D. Gaulin, Octupolar versus n el order in cubic $5d^2$ double perovskites, *Physical Review Letters* **124**, 087206 (2020).
 - [50] S. Voleti, D. D. Maharaj, B. D. Gaulin, G. Luke, and A. Paramakanti, Multipolar magnetism in d-orbital systems: Crystal field levels, octupolar order, and orbital loop currents, *Physical Review B* **101**, 155118 (2020).
 - [51] S. Voleti, K. Pradhan, S. Bhattacharjee, T. Saha-Dasgupta, and A. Paramakanti, Probing octupolar hidden order via janus impurities, *npj Quantum Materials* **8**, 42 (2023).
 - [52] K. Pradhan, A. Paramakanti, and T. Saha-Dasgupta, Multipolar magnetism in $5d^2$ vacancy ordered halide double perovskites, *arXiv preprint arXiv:2403.05633* (2024).
 - [53] E. E. Morgan, G. T. Kent, A. Zohar, A. ODea, G. Wu, A. K. Cheetham, and R. Seshadri, Hybrid and inorganic vacancy-ordered double perovskites A_2WCl_6 , *Chemistry of Materials* **35**, 7032 (2023).
 - [54] A. Eckardt and E. Anisimovas, High-frequency approximation for periodically driven quantum systems from a floquet-space perspective, *New journal of physics* **17**, 093039 (2015).
 - [55] J. R. Chamorro, L. Ge, J. Flynn, M. A. Subramanian, M. Mourigal, and T. M. McQueen, Frustrated spin one on a diamond lattice in NiRh_2O_4 , *Phys. Rev. Mater.* **2**, 034404 (2018).
 - [56] G. Chen, Quantum paramagnet and frustrated quantum criticality in a spin-one diamond lattice antiferromagnet, *Phys. Rev. B* **96**, 020412 (2017).
 - [57] Y. H. Wang, H. Steinberg, P. Jarillo-Herrero, and N. Gedik, Observation of floquet-bloch states on the surface of a topological insulator, *Science* **342**, 453 (2013), <https://www.science.org/doi/pdf/10.1126/science.1239834>.
 - [58] M. Merboldt, M. Schler, D. Schmitt, J. P. Bange, W. Bennecke, K. Gadge, K. Pierz, H. W. Schumacher, D. Momeni, D. Steil, S. R. Manmana, M. Sentef, M. Reutz, and S. Mathias, Observation of floquet states in graphene (2024), *arXiv:2404.12791 [cond-mat.mes-hall]*.
 - [59] D. Choi, M. Mogi, U. D. Giovannini, D. Azoury, B. Lv, Y. Su, H. Hbener, A. Rubio, and N. Gedik, Direct observation of floquet-bloch states in monolayer graphene (2024), *arXiv:2404.14392 [cond-mat.mes-hall]*.
 - [60] C. Hua, D. A. Tennant, A. T. Savici, V. Sedov, G. Sala, and B. Winn, Implementation of a laserneutron pumpprobe capability for inelastic neutron scattering, *Review of Scientific Instruments* **95**, 033902 (2024), https://pubs.aip.org/aip/rsi/article-pdf/doi/10.1063/5.0181310/19712332/033902_1.5.0181310.pdf.

Supplementary Material: Phonon-driven multipolar dynamics in spin-orbit coupled Mott insulators

Kathleen Hart,^{1,*} Ruairidh Sutcliffe,^{1,*} Gil Refael,^{2,3} and Arun Paramekanti^{1,†}

¹*Department of Physics, University of Toronto, 60 St. George Street, Toronto, ON, M5S 1A7 Canada*

²*Department of Physics, California Institute of Technology, Pasadena CA 91125, USA*

³*Institute for Quantum Information and Matter,
California Institute of Technology, Pasadena CA 91125, USA*

(Dated: May 7, 2024)

I. DETAILS OF $SU(N)$ MONTE CARLO AND MOLECULAR DYNAMICS OF SPINS AND PHONONS

In this section we discuss the $SU(N)$ Monte Carlo (MC) and molecular dynamics (MD) simulations developed for this work. Explicitly, the Monte Carlo simulations broadly follow those discussed in Ref.[1], where, in contrast to traditional vector Monte Carlo, where spin expectation values of observables are updated directly, we instead perform updates of N dimensional complex vectors representative of the local wavefunctions. Consequently, Monte Carlo updates are performed, in the spin-1/2 and spin-1 case, by representing the wavefunction of the full lattice as a direct product $|\Psi\rangle = \otimes_{\mathbf{r}} |\psi_{\mathbf{r}}\rangle$ [2]

$$\text{Spin } 1/2 : |\psi_{\mathbf{r}}\rangle = a|+1/2\rangle + b|-1/2\rangle, \quad (1)$$

$$\text{Spin } 1 : |\psi_{\mathbf{r}}\rangle = a|+1\rangle + b|0\rangle + c|-1\rangle, \quad (2)$$

where \mathbf{r} indexes the site and a, b and c are complex parameters, constrained by the normalization of the wavefunction and the irrelevance of a global phase. For MC simulations of the spin system, we sample the wavefunctions with the weight $P \propto e^{-\langle H_{\text{sp}} \rangle / T}$ where the average is computed using $|\Psi\rangle$. For the full spin-phonon Hamiltonian, the MC simulations sample the spin wavefunction $|\psi_{\mathbf{r}}\rangle$ and phonon phase space $(Q_{\alpha}(\mathbf{r}), P_{\alpha}(\mathbf{r}))$ at each site \mathbf{r} , with weights $P \propto e^{-[\langle H_{\text{sp}} \rangle + \langle H_{\text{sp-ph}} \rangle + H_{\text{ph}}] / T}$. Since the phonons are treated classically, the phonon momenta can be integrated out and we only sample phonon coordinates Q_{α} and spins in the equilibrium Monte Carlo simulations.

Simulations are generally termed $SU(N)$, where $N = 2S + 1$, for a spin- S system, since, using the aforementioned wavefunctions, one can track the expectation values of all $N^2 - 1$ generators of the representation. From linear combinations thereof, all dipolar and *multipolar* expectation values may be constructed. For $S = 1/2$, we have $N = 2$ and the three generators of the representation are just the Pauli matrices. The resulting simulations are equivalent to traditional vector Monte Carlo simulations. For MC updates in these simulations, we update both the spin wavefunctions and phonon coordinates using a Metropolis update scheme. We select an upper bound Q_{max} for the phonon coordinates at each site/mode and sample from $[-Q_{\text{max}}, Q_{\text{max}}]$. In suitable units (see below), we pick $Q_{\text{max}} = 10a$ (which corresponds to a cutoff strain of $\sim 10\%$ of the lattice constant).

For simulations of the dynamics at any initial temperature T , we use a large number of equilibrated Monte Carlo configurations for spin wavefunctions and phonon coordinates (typically ~ 100 -300), and pick initial phonon momenta from a Boltzmann distribution at temperature T . These initial configurations are evolved according to the Schrodinger equation for the spin state and Newton's laws for $\{Q, P\}$. Our specific implementation of the MD simulations uses the Schrodinger midpoint method discussed in Ref.[3], with the added caveat that we necessarily update both phonon coordinates and momenta via a matching midpoint scheme. We have tested this method to ensure energy and spin length conservation and other multipolar operator trace constraints.

II. DETAILS OF THE PSEUDOSPIN-1/2 MODEL

A. Choice of model parameters in the Hamiltonian

In this section we provide further details and justification for the parameters used in the main text for Mott insulators with a non-Kramers doublet. We begin with the full Hamiltonian $H = H_{\text{sp}} + H_{\text{ph}} + H_{\text{sp-ph}}$ given in the

* These authors contributed equally to this work.

† arun.paramekanti@utoronto.ca

main text. Here,

$$H_{\text{sp}} = \sum_{\langle \mathbf{r}, \mathbf{r}' \rangle} [-J_0 \tau_{\mathbf{r}y} \tau_{\mathbf{r}'y} + J_1 (\cos^2 \phi_{\mathbf{r}\mathbf{r}'} + \gamma \sin^2 \phi_{\mathbf{r}\mathbf{r}'}) \tau_{\mathbf{r}z} \tau_{\mathbf{r}'z} + J_1 (1 - \gamma) \sin \phi_{\mathbf{r}\mathbf{r}'} \cos \phi_{\mathbf{r}\mathbf{r}'} (\tau_{\mathbf{r}x} \tau_{\mathbf{r}'z} + \tau_{\mathbf{r}z} \tau_{\mathbf{r}'x}) + J_1 (\sin^2 \phi_{\mathbf{r}\mathbf{r}'} + \gamma \cos^2 \phi_{\mathbf{r}\mathbf{r}'}) \tau_{\mathbf{r}x} \tau_{\mathbf{r}'x}]. \quad (3)$$

The spin Hamiltonian has dimensionless ratios of exchange couplings J_1/J_0 and γ [4, 5]. Based on density functional theory and dynamical mean field theory for $\text{Ba}_2\text{CoOsO}_6$ [6], $\gamma \approx -0.4$ and $J_1/J_0 \approx 0.5$; this places us in the ferro-octupolar phase for $T/J_0 \lesssim 3.2$ as determined from classical Monte Carlo simulations [5]. Choosing $J_0 \approx 1$ meV leads to $T_{\text{oct}} \approx 40$ K which is in the right ballpark for experimental results on $\text{Ba}_2\text{CoOsO}_6$ [5, 7]. Motivated by constructing the more general phase diagram of this model, we have fixed γ and chosen to vary J_1/J_0 and T/J_0 which allows us to access both ferro-octupolar and quadrupolar ordered phases as shown in Fig.1 of the manuscript.

The phonon Hamiltonian and spin-phonon couplings are given by

$$H_{\text{ph}} = \sum_{\mathbf{r}, \alpha=x,z} \left[\frac{1}{2} M \Omega^2 Q_{\alpha}^2(\mathbf{r}) + \frac{1}{2M} P_{\alpha}^2(\mathbf{r}) \right], \quad (4)$$

$$H_{\text{sp-ph}} = -\lambda \sum_{\mathbf{r}} [Q_x(\mathbf{r}) \tau_{\mathbf{r}x} + Q_z(\mathbf{r}) \tau_{\mathbf{r}z}] \quad (5)$$

We go to dimensionless variables for $H_{\text{sp}} + H_{\text{ph}} + H_{\text{sp-ph}}$ by using a typical length scale a for phonon displacements and dividing by the dominant spin exchange energy scale J_0 . This leads to the dimensionless Hamiltonian for terms involving the phonons as

$$H_{\text{ph}}/J_0 = \sum_{\mathbf{r}, \alpha=x,z} [g_1 \bar{P}_{\alpha}^2(\mathbf{r}) + g_2 \bar{Q}_{\alpha}^2(\mathbf{r})], \quad (6)$$

$$H_{\text{sp-ph}}/J_0 = g_3 \sum_{\mathbf{r}} [\bar{Q}_x(\mathbf{r}) \tau_{\mathbf{r}x} + \bar{Q}_z(\mathbf{r}) \tau_{\mathbf{r}z}] \quad (7)$$

where the dimensionless coupling constants are

$$g_1 = \frac{\hbar^2}{2M J_0 a^2}; \quad g_2 = \frac{M \Omega^2 a^2}{2J_0 \hbar^2}; \quad g_3 = \lambda a / J_0 \quad (8)$$

We set $a = 0.04 \text{ \AA}$, so that $\bar{Q}_{\alpha} = 1$ corresponds to an approximately 1% dynamical strain (since the typical crystal lattice constant for the double perovskites is $\approx 4 \text{ \AA}$). To estimate g_1, g_2, g_3 , we fix $M = m_{\text{oxygen}} \approx 2.6 \times 10^{-26} \text{ kg}$, $\Omega \approx 80 \text{ meV}$ as a typical \mathcal{E}_g phonon mode frequency, and fix the ferro-octupolar exchange coupling $J_0 = 1 \text{ meV}$ which yields the ferro-octupolar transition temperature $T_{\text{oct}} \approx 40 \text{ K}$ [5, 6]. This leads to $g_1 \approx 80$, $g_2 \approx 20$. Density functional theory shows that an approximately 1% strain leads to a splitting $\sim 5 \text{ meV}$ splitting of the non-Kramers doublet [7]; this translates to a dimensionless spin-phonon coupling $g_3 \approx 5$.

B. Spin and phonon dynamics for pump-probe simulations

1. Ferro-octupolar phase

In this section we provide plots showing the accompanying spin dynamics for the pump-probe simulations shown in the main text. Specifically, Fig. 1(b) of the main text demonstrates a Hall-like effect in the \mathcal{E}_g phonons of the pseudospin-1/2 model for $T < T_{\text{oct}}$, where an initial momentum kick to the Q_x phonons transfers energy through the pseudospins to the Q_z phonon and back again to Q_x , through the pseudospins. Figs. S1(a) and (b) in the ferro-octupolar phase (for $T < T_{\text{oct}}$) show the corresponding dynamics of the pseudospin components τ_x, τ_z averaged over the lattice and over ~ 80 initial configurations where $\langle \tau_y \rangle > 0$. While $\tau_y \approx 1$ (not shown), there are rapid oscillations in τ_x, τ_z which follow the phonon frequency, as well as slower oscillations which arise from spin precession around τ_y direction as clearly seen from the envelope. Figs. S1(c) and (d) show the short time dynamics of the phonon modes which is plotted over longer timescales in Fig. 1(b) of the main manuscript where the rapid oscillations are not resolved.

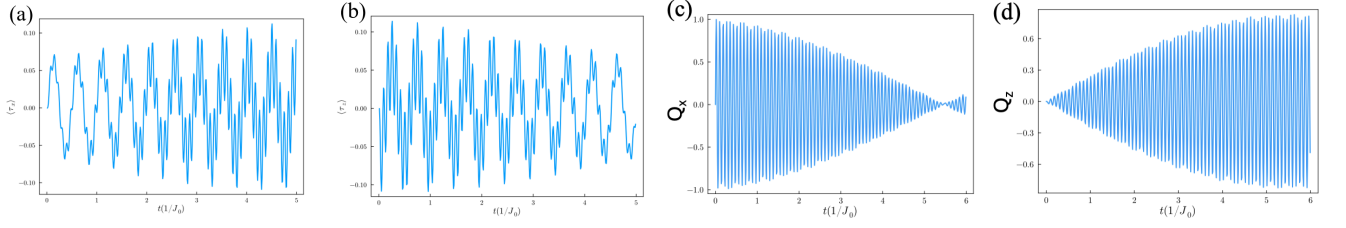


FIG. S1. Spin dynamics and short-time phonon dynamics in the ferro-octupolar phase corresponding to parameters in Fig. 1(b) of main manuscript ($T < T_{\text{oct}}$, left panel). We observe small, coherent rapid oscillation in the (a) τ_x and (b) τ_z components which track the phonons to which they are coupled, in addition to slower oscillation which correspond to the timescale governed by J_0 . Short time phonon dynamics reveals the rapid oscillations of (c) Q_x and (d) Q_z averaged over 80 configurations.

2. Paramagnetic phase

In the paramagnetic phase ($T > T_{\text{oct}}$), Fig. 1(b) of the main manuscript shows that oscillatory phonon energy transfer between Q_x and Q_z is absent. In the accompanying plot, Figs.S2(a) and (b) show the spin responses in the paramagnetic phase which displays no coherent long-lived spin oscillations unlike in the ferro-octupolar phase. Similarly, while the driven phonon component Q_x shows weakly damped oscillations in Fig.S2(c), there is only a very small oscillatory amplitude induced in Q_z as seen in Fig.S2(d) (see scale), which we attribute to finite size effects.

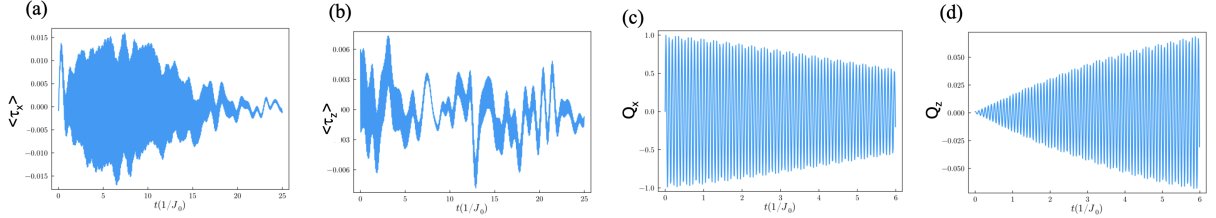


FIG. S2. Spin dynamics and short-time phonon dynamics in the paramagnetic phase corresponding to parameters in Fig. 1(b) of main manuscript ($T > T_{\text{oct}}$, right panel). We observe rapid dephasing of oscillation in the (a) τ_x and (b) τ_z components. Short time phonon dynamics reveals the rapid oscillations of (c) pumped phonon Q_x and (d) only weak transfer of energy to Q_z phonon mode resulting in very weak amplitude oscillations, which we expect to vanish with increasing system size.

3. Antiferroquadrupolar phase

We now present the phonon dynamics of pump-probe simulations conducted in the antiferroquadrupolar (AFQ) regime with $J_1/J_0 = 2.0$, similar to those presented in the two panels of Fig. 1(b) in the main text. Explicitly here, we show points at $T/J_0 = 0.5$, well below the transition temperature, T_{AFQ} , and above T_{AFQ} at $T/J_0 = 4.5$. Unlike in the case of octupolar order, there is no significant coherent energy transfer between the kicked, Q_x , phonon and Q_z phonon either above or below the quadrupolar transition temperature as seen from Fig. S3(a) and Fig. S3(b).

C. Mean field model of coupled pseudospin and phonon dynamics in the octupolar phase

1. Pseudospin dynamics

In this section, we consider a single spin in a ferro-octupolar ordered state with a phonon mode Q_x coupled to τ_x . We construct such a model in order to simulate the effect of a single phonon pump in the pseudospin-1/2 model as a potential mechanism by which the phonon cross-amplitude shown in Fig. 1 of the main text, is induced. Here, we model the effect of nearest-neighbour pseudospin interactions as a constant octupolar Weiss mean field h pointing along τ_y , and the pumped phonon as a sinusoidal time-dependent drive. Thus, the single spin Hamiltonian is:

$$H = -h\tau_y - A_{\text{eff}} \sin(\Omega t + \varphi)\tau_x, \quad (9)$$

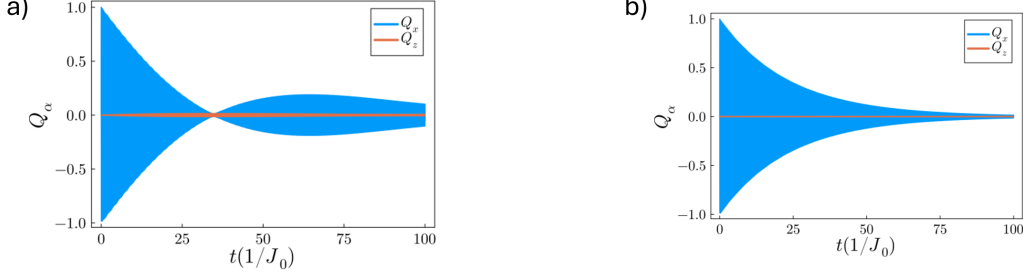


FIG. S3. Phonon, Q_x and Q_z , dynamics for a pump-probe simulation in the AFQ ordered regime, with $J_1/J_0 = 2.0$ at (a) $T/J_0 = 0.5$ and (b) $T/J_0 = 4.5$, averaged over 160 configurations. Here, we initially give a momentum to kick to the Q_x phonon but see no significant coherent transfer of energy between the Q_x and Q_z phonons.

where $A_{\text{eff}} = \lambda Q_0$ encompasses the spin-phonon coupling strength λ and the phonon amplitude Q_0 . The Heisenberg equations of motion may thus be written as:

$$\dot{\tau}_x = -h\tau_z \quad (10)$$

$$\dot{\tau}_y = A_{\text{eff}} \sin(\Omega t + \varphi) \tau_z \quad (11)$$

$$\dot{\tau}_z = h\tau_x - A_{\text{eff}} \sin(\Omega t + \varphi) \tau_y. \quad (12)$$

Given that fluctuations away from the ferro-octupolar ordering are small, we make the simplifying approximation that $\tau_y \simeq 1$ and is constant in time. Therefore, the equations of motion reduce to:

$$\dot{\tau}_x = -h\tau_z \quad (13)$$

$$\dot{\tau}_z = h\tau_x - A_{\text{eff}} \sin(\Omega t + \varphi). \quad (14)$$

Solving these coupled equations with the initial conditions $\tau_x(0) = \tau_x^0$ and $\tau_z(0) = \tau_z^0$, we find

$$\tau_x(t) = \left(\tau_x^0 + \frac{A_{\text{eff}} h \sin \varphi}{\Omega^2 - h^2} \right) \cos(ht) + \left(-\tau_z^0 + \frac{A_{\text{eff}} \Omega \cos(\varphi)}{\Omega^2 - h^2} \right) \sin(ht) - \frac{A_{\text{eff}} h}{\Omega^2 - h^2} \sin(\Omega t + \varphi) \quad (15)$$

$$\tau_z(t) = \left(\tau_x^0 + \frac{A_{\text{eff}} h \sin(\varphi)}{\Omega^2 - h^2} \right) \sin(ht) + \left(\tau_z^0 - \frac{A_{\text{eff}} \Omega \cos(\varphi)}{\Omega^2 - h^2} \right) \cos(ht) + \frac{A_{\text{eff}} \Omega}{\Omega^2 - h^2} \cos(\Omega t + \varphi) \quad (16)$$

Fig. S4 plots the dynamics in Eq. 15 and Eq.16, and it shows two key features: a slower oscillation which comes from

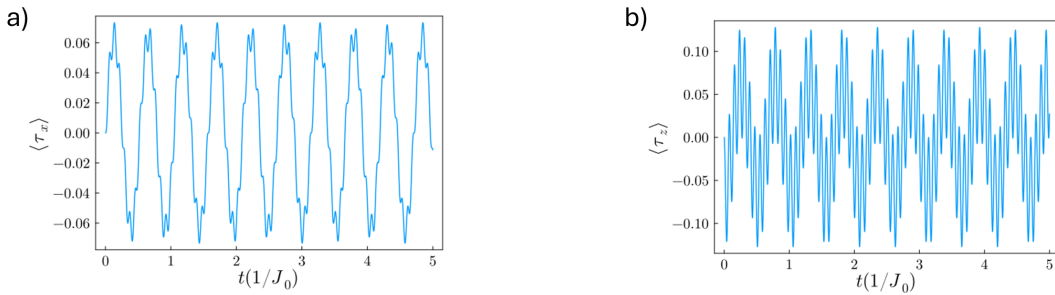


FIG. S4. Analytical solution to the coupled differential equations given by Eqs. 15, shown in a), and 16, shown in b). We use parameters as in the numerical pump-probe simulations, namely $A_{\text{eff}} = 5$, $\Omega = 80$, $h = 12$, and $\phi = 0$, with initial conditions $\tau_x^0 = \tau_z^0 = 0$. The plots resemble the short-time dynamics presented in Fig. S1.

the precession of the spins about the local magnetic field (on timescale $\sim 0.5/J_0$), on which is superposed a rapid oscillation that results from the linear coupling of the fast phonon coordinate to the spin components (on timescale $\sim 0.1/J_0$).

2. Phonon dynamics

Using the previous section as a starting point, we may compute the back-action on the phonon degrees of freedom to capture the phonon dynamics shown in Fig. S1. Explicitly, if we treat the spin equations of motion shown in Eqs. 15 and 16 as a driving term through the spin-phonon coupling, and note that the dominant effect of this drive will be due to the terms resonant with the phonon frequency Ω , we may reduce this problem to that of a driven damped harmonic oscillator. Explicitly, one can write:

$$\frac{dQ_x}{dt} = P_x/M \quad (17)$$

$$\frac{dQ_z}{dt} = P_z/M \quad (18)$$

$$\frac{dP_x}{dt} = -M\Omega^2 Q_x + \frac{\lambda A_{\text{eff}} h}{\Omega^2 - h^2} \sin(\Omega t) - \eta P_x \quad (19)$$

$$\frac{dP_z}{dt} = -M\Omega^2 Q_z - \frac{\lambda A_{\text{eff}} \Omega}{\Omega^2 - h^2} \cos(\Omega t) - \eta P_z \quad (20)$$

where the coefficients in, suitably normalized units, are chosen as discussed previously. Thus, we may then write the trajectories of the Q_x and Q_z phonons as:

$$Q_\alpha(t) = D_\alpha e^{-\eta t/2} \sin(\Omega' t + \Phi_h^\alpha) + C_\alpha \cos(\Omega t - \Phi) \quad (21)$$

using the initial conditions $Q_\alpha(0) = 0.0, 0.0$ and $P_\alpha(0) = 1.0, 0.0$ for the Q_x and Q_z phonons, respectively. Here, $\Phi = \pi/2 - \phi_D$, $\Omega' = \sqrt{\Omega^2 - (\eta/2)^2}$, $\Phi_h^\alpha = \arctan\left(\frac{\Omega' C_\alpha \cos(\Phi)}{P_0/M + (\eta/2)(C_\alpha \cos(\Phi)) - C_\alpha \Omega \sin(\Phi)}\right)$, $C_\alpha = F_0^\alpha/\eta M \Omega$, and $D_\alpha = C_\alpha \cos(\Phi)/\sin(\Phi_h^\alpha)$. F_0^α are the driving amplitudes shown in Eqs. 19 and 20, and $\phi_D = \pi/2, 0$ for Q_x and Q_z respectively. The analytical results for Q_x and Q_z are shown in Fig. S5 and qualitatively agree with the dynamics seen in the full lattice model, Fig. S1.

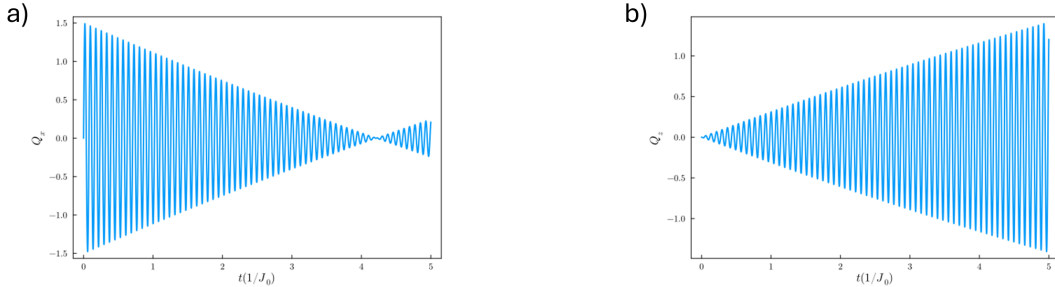


FIG. S5. Analytical solution to the coupled differential equations given by 21 for Q_x , shown in a), and Q_z , shown in b). We use parameters discussed in the text with the initial conditions: $Q_x(0) = Q_z(0) = 0.0$ and $P_x(0) = 1.0, P_z(0) = 0.0$. The plots resemble the short-time dynamics presented in Fig. S1.

D. Domain wall dynamics in octupolar phase

In this section, we construct a simplified model for the mechanism of octupolar order switching seen in the full pseudospin-1/2 model discussed in the main text. We begin by simulating spins sitting at or near *domain walls* using a mean field description. Explicitly, we do this by initializing the spin of interest close to the xz plane. Further, to this end, we may also assume that the effective field produced by neighboring spins sitting on either side of the domain wall will cancel out. Thus, the only contributors to the effective field in τ_y are neighboring spins which similarly sit

on the domain wall and each contribute an effective field approximately equal to the τ_y component of the spin of interest. We may thus write our Hamiltonian as:

$$H = -h(t)\tau_y - A_{\text{eff}} \cos(\Omega t)\tau_x - A_{\text{eff}} \cos(\Omega t - \phi)\tau_z, \quad (22)$$

where $h(t) \propto \langle \tau_y \rangle(t)$, where $\langle \tau_y \rangle(t)$ represents the expectation value of τ_y for the single spin which we are simulating, Ω is the phonon frequency, and $A_{\text{eff}} = \lambda Q_0$ with Q_0 being the phonon amplitude and λ being the spin-phonon coupling. We then simulated two near-domain wall conditions, explicitly, looking at both sides of a domain wall with $\langle \tau_y \rangle > 0$ and $\langle \tau_y \rangle < 0$. These spins were then driven using a two phonon drive as described in Eq.22, with phonon parameters matching those used in the full model ($A_{\text{eff}}/J_0 \sim 5$, $\Omega/J_0 \sim 80$) and $\phi = \pm\pi/2$ depending on the initial state to induce octupolar order switching in both cases. The results are shown in Figure S6.

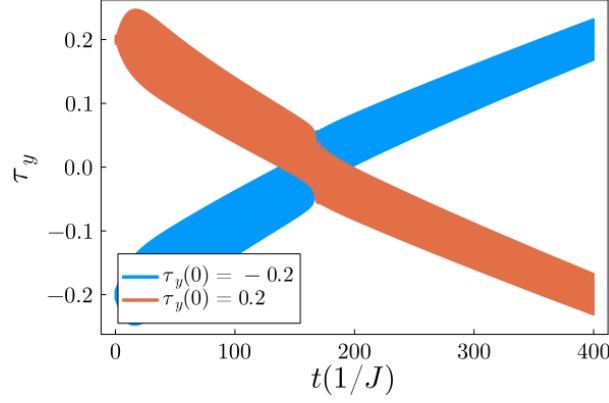


FIG. S6. Toy model of a driven spin, starting near the xz plane, with a time dependent field in τ_y with a two phonon sinusoidal drive. Here, the phonons are driven $\pi/2$ out of phase and coupled to the τ_x and τ_z spin components respectively. Spin trajectories for states having initial $\langle \tau_y \rangle = \pm 0.2$ are shown where the state with $\langle \tau_y(0) \rangle = +0.2$ was driven with $\phi = \pi/2$, while the state with $\langle \tau_y(0) \rangle = -0.2$ was driven with $\phi = -\pi/2$.

III. DETAILS OF THE SPIN-1 MODEL

A. Spin-1 multipoles, commutators, and Gell-Mann matrices

In this section, we introduce a number of useful definitions for the spin-1 model described in this work. Using the dipolar spin operators S_x, S_y and S_z which satisfy the usual $SU(2)$ algebra, we define quadrupolar operators which are quadratic in the spin-1 operators and may be arranged into traceless tensors:

$$T_{xy} = S_x S_y + S_y S_x \quad (23)$$

$$T_{xz} = S_x S_z + S_z S_x \quad (24)$$

$$T_{yz} = S_y S_z + S_z S_y \quad (25)$$

$$T_{x^2-y^2} = S_x^2 - S_y^2 \quad (26)$$

$$T_{z^2} = \frac{1}{\sqrt{3}}(3S_z^2 - 2) \quad (27)$$

We have set the normalization of all dipole and quadrupole operators \mathcal{O} so they all have $\text{Tr}(\mathcal{O}^2) = 2$. The full set of commutation relations is given by

Dipole-Dipole:

$$[S_x, S_y] = iS_z; \quad [S_y, S_z] = iS_x; \quad [S_z, S_x] = iS_y \quad (28)$$

Quadrupole-Quadrupole:

$$\begin{aligned} [T_{xy}, T_{xz}] &= iS_x & [T_{xy}, T_{yz}] &= -iS_y & [T_{xy}, T_{x^2-y^2}] &= -2iS_z & [T_{xy}, T_{z^2}] &= 0 \\ [T_{xz}, T_{yz}] &= iS_z & [T_{xz}, T_{x^2-y^2}] &= iS_y & [T_{xz}, T_{z^2}] &= -\sqrt{3}iS_y \\ [T_{yz}, T_{x^2-y^2}] &= iS_x & [T_{yz}, T_{z^2}] &= \sqrt{3}iS_x \\ [T_{x^2-y^2}, T_{z^2}] &= 0, \end{aligned} \quad (29)$$

Quadrupole-Dipole:

$$\begin{aligned}
[S_x, T_{xy}] &= iT_{xz} & [S_x, T_{xz}] &= -iT_{xy} & [S_x, T_{yz}] &= i(\sqrt{3}T_{z^2} + T_{x^2-y^2}) & [S_x, T_{x^2-y^2}] &= -iT_{yz} & [S_x, T_{z^2}] &= -i\sqrt{3}T_{yz} \\
[S_y, T_{xy}] &= -iT_{yz} & [S_y, T_{xz}] &= -i(\sqrt{3}T_{z^2} - T_{x^2-y^2}) & [S_y, T_{yz}] &= iT_{xy} & [S_y, T_{x^2-y^2}] &= -iT_{xz} & [S_y, T_{z^2}] &= i\sqrt{3}T_{xz} \\
[S_z, T_{xy}] &= -iT_{x^2-y^2} & [S_z, T_{xz}] &= iT_{yz} & [S_z, T_{yz}] &= -iT_{xz} & [S_z, T_{x^2-y^2}] &= iT_{xy} & [S_z, T_{z^2}] &= 0.
\end{aligned} \tag{30}$$

While there are, naturally, a large number of individual commutation relations, it is important to note that there are a number of closed loops that we have made use of in the parts of this work concerning the spin-1 model. Specifically, one may note that the commutation relations of:

- T_{xz}, T_{yz} , and S_z
- S_y, T_{xz} , and $\sqrt{3}T_{z^2} - T_{x^2-y^2}$,
- S_x, T_{yz} , and $\sqrt{3}T_{z^2} + T_{x^2-y^2}$,

are each respectively self-contained.

We also present the generators used in the $SU(3)$, $S = 1$, simulations in this work. Explicitly, to this end, we use the Gell-Mann matrices:

$$\begin{aligned}
\lambda_1 &= \begin{pmatrix} 0 & 1 & 0 \\ 1 & 0 & 0 \\ 0 & 0 & 0 \end{pmatrix} & \lambda_2 &= \begin{pmatrix} 0 & -i & 0 \\ i & 0 & 0 \\ 0 & 0 & 0 \end{pmatrix} & \lambda_3 &= \begin{pmatrix} 1 & 0 & 0 \\ 0 & -1 & 0 \\ 0 & 0 & 0 \end{pmatrix} & \lambda_4 &= \begin{pmatrix} 0 & 0 & 1 \\ 0 & 0 & 0 \\ 1 & 0 & 0 \end{pmatrix} \\
\lambda_5 &= \begin{pmatrix} 0 & 0 & -i \\ 0 & 0 & 0 \\ i & 0 & 0 \end{pmatrix} & \lambda_6 &= \begin{pmatrix} 0 & 0 & 0 \\ 0 & 0 & 1 \\ 0 & 1 & 0 \end{pmatrix} & \lambda_7 &= \begin{pmatrix} 0 & 0 & 0 \\ 0 & 0 & -i \\ 0 & i & 0 \end{pmatrix} & \lambda_8 &= \frac{1}{\sqrt{3}} \begin{pmatrix} 1 & 0 & 0 \\ 0 & 1 & 0 \\ 0 & 0 & -2 \end{pmatrix}
\end{aligned}$$

Since we find it useful in our $SU(3)$ simulations [1, 8], we also present the decomposition of spin-1 dipole and quadrupole operators into a linear combination of the Gell-Mann matrices:

$$\begin{aligned}
S_x &= \frac{1}{\sqrt{2}}(\lambda_4 + \lambda_6) & S_y &= \frac{1}{\sqrt{2}}(\lambda_5 - \lambda_7) & S_z &= \lambda_3 \\
T_{xy} &= \lambda_2 & T_{xz} &= \frac{1}{\sqrt{2}}(\lambda_4 - \lambda_6) & T_{yz} &= \frac{1}{\sqrt{2}}(\lambda_5 + \lambda_7) \\
T_{x^2-y^2} &= \lambda_1 & T_{z^2} &= \lambda_8.
\end{aligned}$$

B. Driven spin-1 Magnus expansion in the antiferromagnetic phase

In this section, we compute the Magnus expansion for the single phonon drive in the antiferromagnetic phase for the spin-1 model, with the goal of understanding the difference, at low energy, between the dynamic spin structure factor in the undriven and single-phonon-driven cases. Explicitly, we may begin with the Hamiltonian:

$$H = J \sum_{\langle \mathbf{r}\mathbf{r}' \rangle} \mathbf{S}(\mathbf{r}) \cdot \mathbf{S}(\mathbf{r}') + D \sum_{\mathbf{r}} S_z^2(\mathbf{r}) + A_{\text{eff}} \sum_{\mathbf{r}} \cos(\Omega t) T_{xz}(\mathbf{r}), \tag{31}$$

where A encompasses the phonon amplitude and spin-phonon coupling strength and Ω is the phonon frequency, where we have approximated the xz phonon by its sinusoidal drive. From here, one may easily identify the Fourier components of the time-dependent Hamiltonian:

$$H_0 = J \sum_{\langle \mathbf{r}\mathbf{r}' \rangle} \mathbf{S}(\mathbf{r}) \cdot \mathbf{S}(\mathbf{r}') + D \sum_{\mathbf{r}} S_z^2(\mathbf{r}),$$

and

$$H_1 = H_{-1} = \frac{A_{\text{eff}}}{2} \sum_{\mathbf{r}} T_{xz}(\mathbf{r}).$$

We thus see that

$$H_{\text{eff}}^{(0)} = H_0 = J \sum_{\langle \mathbf{r}\mathbf{r}' \rangle} S(\mathbf{r})S(\mathbf{r}') + D \sum_{\mathbf{r}} S_z(\mathbf{r})^2$$

$$H_{\text{eff}}^{(1)} = 0$$

$$H_{\text{eff}}^{(2)} = -\frac{5}{3\Omega^2} \sum_{\langle \mathbf{r}\mathbf{r}' \rangle} \left(\frac{A_{\text{eff}}^2 J}{4} S_x(\mathbf{r})S_x(\mathbf{r}') + A_{\text{eff}}^2 J S_y(\mathbf{r})S_y(\mathbf{r}') + \frac{A_{\text{eff}}^2 J}{4} S_z(\mathbf{r})S_z(\mathbf{r}') \right) + \frac{A_{\text{eff}}^2 D}{4} \sum_{\mathbf{r}} T_{\text{eg}}(\mathbf{r})$$

where $T_{\text{eg}}(\mathbf{r}) \equiv \sqrt{3}T_{z^2}(\mathbf{r}) - T_{x^2-y^2}(\mathbf{r})$. Thus, we may write

$$H_{\text{eff}} \simeq J \sum_{\langle \mathbf{r}\mathbf{r}' \rangle} \left[\left(1 - \frac{5A_{\text{eff}}^2}{12\Omega^2} \right) S_x(\mathbf{r})S_x(\mathbf{r}') + \left(1 - \frac{5A_{\text{eff}}^2}{3\Omega^2} \right) S_y(\mathbf{r})S_y(\mathbf{r}') + \left(1 - \frac{5A_{\text{eff}}^2}{12\Omega^2} \right) S_z(\mathbf{r})S_z(\mathbf{r}') \right] \\ + D \sum_{\mathbf{r}} \left[\left(1 - \frac{5A_{\text{eff}}^2}{4\Omega^2} \right) S_z^2(\mathbf{r}) + \frac{5A_{\text{eff}}^2}{12\Omega^2} T_{x^2-y^2}(\mathbf{r}) + \frac{5A_{\text{eff}}^2}{6\Omega^2} I \right] + \dots \quad (32)$$

One can see here, that the single phonon drive acts to renormalize both the exchange constant J , in addition to the single-ion anisotropy constant D . This effect is visible in the dynamical spin structure factor (DSSF) data shown in Fig. 4(b) of the main text, wherein the three bands computed for the static case are shifted down as a consequence of the one-phonon drive. Explicitly, using numbers for the parameters $A_{\text{eff}} \simeq 5$ and $\Omega \simeq 40$, one can estimate the renormalization of S_x and S_z components of J to be $\sim 0.7\%$, with the renormalization of D and the S_y component of J being $\sim 2.1\%$ and $\sim 2.8\%$ respectively.

C. Dynamical spin structure factor for the spin-1 model

To study the effect of driving on flavor-wave excitations, we calculate the dynamical spin structure factor (DSSF) in the antiferromagnetic regime, in which $J/D = 0.4$ and $T/J = 0.3$. First, we compute the spatial Fourier transform of the spin components

$$S_{\alpha}(\mathbf{q}, t) = \frac{1}{\sqrt{N}} \sum_{\mathbf{r}} e^{i\mathbf{q}\cdot\mathbf{r}} S_{\alpha}(\mathbf{r}, t) \quad (33)$$

where $S_{\alpha}(\mathbf{r}, t)$ is the classical spin component and $\alpha = x, y, z$. We then calculate the Fourier transform in time as

$$S_{\alpha}(\mathbf{q}, \omega) = \frac{1}{\sqrt{N_t}} \sum_t e^{i\omega t} S_{\alpha}(\mathbf{q}, t) \quad (34)$$

where N_t is the number of time steps. Finally, since the Fourier transformed spin components are real, then $S_{\alpha}(\mathbf{q}, \omega) = S_{\alpha}^*(-\mathbf{q}, -\omega)$ and we can thus calculate the DSSF as

$$\mathcal{S}(\mathbf{q}, \omega) = \sum_{\alpha} |S_{\alpha}(\mathbf{q}, \omega)|^2 \quad (35)$$

All DSSF data presented both here and in the main text are multiplied by the quantum to classical correspondence $\frac{\beta\omega}{1-e^{-\beta\omega}}$ [8]. We start by calculating the DSSF for our spin-1 model with phonons coupled, but not driven with $dt = 0.1/J$, $N_t = 2000$ and averaging over 200 initial configurations. We find similar features to those reported in Ref. [8], namely two transverse and one longitudinal mode corresponding to in-plane, out-of-plane and dipolar spin length oscillations, respectively. The gapless Goldstone mode arises from the easy-plane antiferromagnetic interaction, in which global rotations of the lattice in the xy plane are energy conserving. The gapped transverse mode results from the single-ion anisotropy which causes fluctuations into the z axis to cost energy.

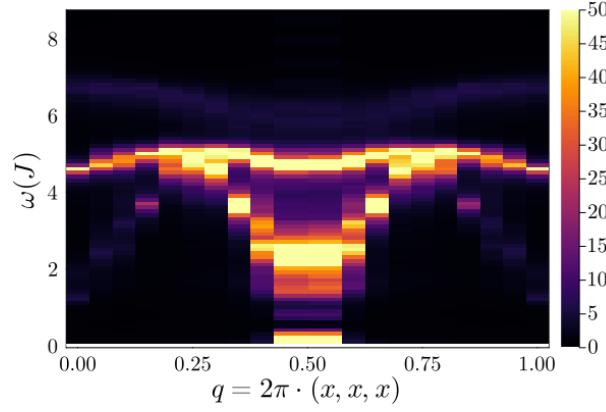


FIG. S7. Flavor-wave dispersion, calculated as $\mathcal{S}(\mathbf{q}, \omega)$, in the AFM phase ($J/D = 0.4$) averaged over 200 configurations to a maximum time $t = 200/J$, with sample spacing $dt = 0.1/J$. There are two transverse modes, one which is Goldstone-like and one which is gapped, and one longitudinal mode. See Fig. 4 in the main text for more details.

D. Driven spin-1 Floquet bands keeping $(0, 0, 0)$, (π, π, π)

In this section we present accompanying dynamical spin structure factor data, for the spin-1 model, to that shown in the main text. Explicitly, in the main text, we show DSSF calculations of the low energy bands and Floquet copies thereof, in the AFM phase. In the plots shown in the main text we remove bright columns arising from equal time correlations. When passing through the zone centre, $q = (\pi, \pi, \pi)$, we expect (and observe) a strong response at all energies due to the underlying antiferromagnetic order present at this wavevector, and thus remove this q point in both the low-energy and Floquet copy DSSF plot. Additionally, in the real time dynamics used to compute the DSSF, we observe uniform (ferromagnetic) oscillation in the x and y spin components, and thus observe accompanying bright spots at both $q = (0, 0, 0)$ and $q = (2\pi, 2\pi, 2\pi)$ at energies $\sim \Omega/J$ (the phonon frequency), which are removed in the DSSF plot of the Floquet copies *only* in the main text. In Fig. S8 we present the DSSF plots of the low energy (left panel) and Floquet excitations (right panel) including the bright ‘stripes’ arising due to equal time correlations.

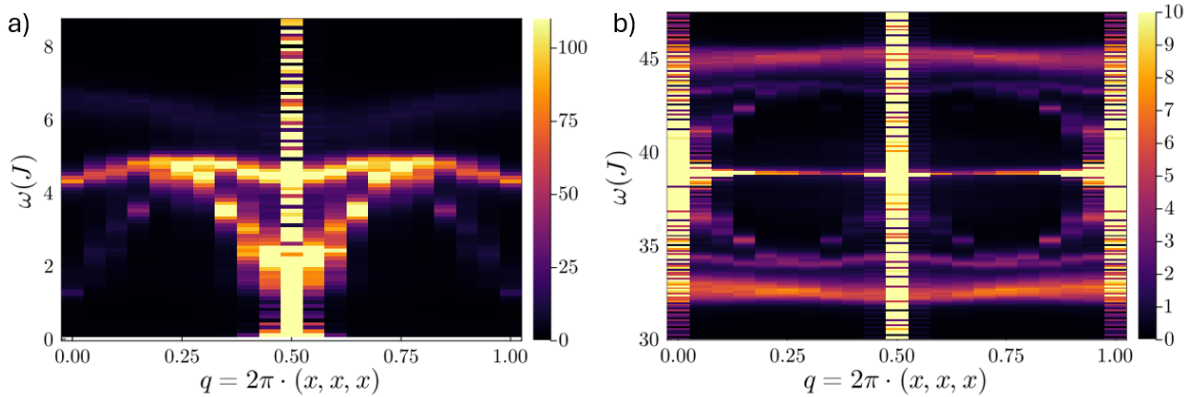


FIG. S8. Flavor-wave dispersion, calculated as $\mathcal{S}(\mathbf{q}, \omega)$, in the AFM regime ($J/D = 0.4$), with a constant drive on the Q_{xz} phonon averaged over 200 configurations to a maximum time $t = 200/J$ with sample spacing $dt = 0.05/J$, where a) shows the low-energy branches and b) shows the Floquet copies about Ω . The ‘stripe’ at the zone center $q = (\pi, \pi, \pi)$, and point $q = (0, 0, 0)$ in the higher energy branches, shows the divergence as a result of the equal time correlator. These points are removed in Fig. 4 presented in the main text.

[1] K. Remund, R. Pohle, Y. Akagi, J. Romhányi, and N. Shannon, Semi-classical simulation of spin-1 magnets, *Physical Review Research* **4**, 033106 (2022).

- [2] E. Stoudenmire, S. Trebst, and L. Balents, Quadrupolar correlations and spin freezing in $s=1$ triangular lattice antiferromagnets, *Physical Review B* **79**, 214436 (2009).
- [3] D. Dahlbom, H. Zhang, C. Miles, X. Bai, C. D. Batista, and K. Barros, Geometric integration of classical spin dynamics via a mean-field schrödinger equation, *Physical Review B* **106**, 054423 (2022).
- [4] A. Paramakanti, D. D. Maharaj, and B. D. Gaulin, Octupolar order in d-orbital mott insulators, *Physical Review B* **101**, 054439 (2020).
- [5] S. Voleti, A. Haldar, and A. Paramakanti, Octupolar order and ising quantum criticality tuned by strain and dimensionality: Application to d-orbital mott insulators, *Physical Review B* **104**, 174431 (2021).
- [6] L. V. Pourovskii, D. F. Mosca, and C. Franchini, Ferro-octupolar order and low-energy excitations in d 2 double perovskites of osmium, *Physical Review Letters* **127**, 237201 (2021).
- [7] S. Voleti, K. Pradhan, S. Bhattacharjee, T. Saha-Dasgupta, and A. Paramakanti, Probing octupolar hidden order via impurity-induced strain, *arXiv preprint arXiv:2211.07666* (2022).
- [8] S.-H. Do, H. Zhang, D. A. Dahlbom, T. J. Williams, V. O. Garlea, T. Hong, T.-H. Jang, S.-W. Cheong, J.-H. Park, K. Barros, *et al.*, Understanding temperature-dependent $su(3)$ spin dynamics in the $s=1$ antiferromagnet $ba_2fesi_2o_7$, *npj Quantum Materials* **8**, 5 (2023).